Hydrol. Earth Syst. Sci. Discuss., 7, 7451–7484, 2010
www.hydrol-earth-syst-sci-discuss.net/7/7451/2010/
doi:10.5194/hessd-7-7451-2010

Hydrology and
Earth System
Sciences
Discussions

Potential of high-resolution detection and retrieval of precipitation fields from X-band spaceborne Synthetic Aperture Radar over land

F. S. Marzano[1,2], S. Mori[1,2], M. Chini[3], L. Pulvirenti[1], N. Pierdicca[1], M. Montopoli[2,5], and J. A. Weinman[4]

[1]Department of Information Engineering, Sapienza University of Rome, Via Eudossiana 18 – 00184 Rome, Italy
[2]Center of Excellence CETEMPS, University of L'Aquila, Italy
[3]Istituto Nazionale di Geofisica e Vulcanologia, Rome, Italy
[4]Department of Atmospheric Sciences, University of Washington, Seattle, Washington, USA
[5]Department of Electric and Information Engineering, University of L'Aquila, L'Aquila, Italy

Received: 23 July 2010 – Accepted: 3 September 2010 – Published: 29 September 2010

Correspondence to: F. S. Marzano (marzano@die.uniroma1.it)

Published by Copernicus Publications on behalf of the European Geosciences Union.

Abstract

X-band Synthetic Aperture Radars (X-SARs), able to image the Earth's surface at metric resolution, may provide a unique opportunity to measure rainfall over land with spatial resolution of about few hundred meters, due to the atmospheric moving-target degradation effects. This capability has become very appealing due to the recent launch of several X-SAR satellites, even though several remote sensing issues are still open. This work is devoted to: (i) explore the potential of X-band high-resolution detection and retrieval of rainfall fields from space using X-SAR signal backscattering amplitude and interferometric phase; (ii) evaluate the effects of spatial resolution degradation by precipitation and inhomogeneous beam filling when comparing to other satellite-based sensors. Our X-SAR analysis of precipitation effects has been carried out using both a TerraSAR-X (TSX) case study of Hurricane "Gustav" in 2008 over Mississippi (USA) and a COSMO-SkyMed (CSK) X-SAR case study of orographic rainfall over Central Italy in 2009. For the TSX case study the near-surface rain rate has been retrieved from the normalized radar cross section by means of a modified regression empirical algorithm (MREA). A relatively simple method to account for the geometric effect of X-SAR observation on estimated rainfall rate and first-order volumetric effects has been developed and applied. The TSX-retrieved rain fields have been compared to those estimated from the Next Generation Weather Radar (NEXRAD) in Mobile (AL, USA). The rainfall detection capability of X-SAR has been tested on the CSK case study using the repeat-pass coherence response and qualitatively comparing its signature with ground-based Mt. Midia C-band radar in central Italy. A numerical simulator to represent the effect of the spatial resolution and the antenna pattern of TRMM satellite Precipitation Radar (PR) and Microwave Imager (TMI), using high-resolution TSX-retrieved rain images, has been also set up in order to evaluate the rainfall beam filling phenomenon. As expected, the spatial average can modify the statistics of the high-resolution precipitation fields, strongly reducing its dynamics in a way non-linearly dependent on the rainrate local average value.

1 Introduction

Nowadays global climate change is of increasing importance both for public opinion, the scientific community, and for its implications on the global economy and life of Earth's inhabitants. From this perspective, a better understanding of the physics of atmospheric processes is required to develop realistic numerical models for analysis and weather forecasting. Precipitation plays a fundamental role within the Earth water cycle and physical hydrology analyses (Dingman, 2002).

Current weather forecast models require high spatial resolution data to be assimilated (Masunaga et al., 2008). Traditional spaceborne passive radiometers have provided global spatial and temporal coverage of precipitation, but they are limited to a spatial resolution of tens of kilometers which tends to wash out convective rain cells and clusters (e.g., Marzano et al., 2002; Tapiador et al., 2004). Moreover, their sensitivity to shallow stratiform rainfall over land is relatively poor at lower microwave frequencies, whereas at higher frequencies observations in presence of frozen hydrometeors are affected by many ambiguities (Bennartz and Petty, 2001). A well-known example of passive microwave radiometer is the TRMM Microwave Imager (TMI) aboard the Tropical Rainfall Measurement Mission (TRMM) satellite. Higher resolution could be obtained by infrared radiometers, but infrared radiance is almost saturated by the presence of precipitating clouds within the observed scene (Tapiador et al., 2004). Spaceborne radar operating at Ku-band (i.e. about 2 cm wavelength) can avoid some of these limitations (Marzano et al., 2002). An example of such a radar is the Precipitation Radar (PR) aboard the TRMM satellite. It has provided unprecedented precipitation measurements over land (Iguchi et al., 2000), but it may miss or underestimate the intensity of shallow precipitation or that from rain cells smaller than 4 km (Durden et al., 1998).

The high spatial resolution of Synthetic Aperture Radars (SARs) operating at X-band (i.e., about 3 cm wavelength) can provide new insights into the structure of precipitating clouds, and it may permit the observation of small precipitation cells at micro-alpha scale between 0.2 and 2 km (Jameson et al., 1997; Melsheimer et al., 1998). The possibility of observing rain cells by means of such sensors have been reported by several authors (e.g. Weinman and Marzano, 2008; Danklmayer et al., 2009; Chandrasekar and Fritz, 2009). Indeed, the nominal spatial resolution of SAR (on the order of meters) is degraded by the turbulent motion of the falling hydrometeors (on the order of hundreds of meters) due to the broadening of the Doppler-frequency spectrum with respect to filters used in fixed-target imaging (Atlas and Moore, 1987). The surface backscattering signal amplitude is mainly affected by rain path attenuation, but it may also depend on the volumetric backscattering of ice hydrometeors (e.g., Weinman and Marzano, 2008; Danklmayer et al., 2009). The received signal phase is influenced by water vapor and liquid hydrometeor distribution through their effect on the atmospheric refractivity and related path delay (Quegan and Lamont, 1986). The slant observation geometry makes the X-SAR atmospheric signature interpretation fairly cumbersome.

Current interest in spaceborne X-SAR measurements is demonstrated by several mission projected or in advanced deployment such as TerraSAR-X (TSX), launched on 2007 by the Deutsches Zentrum fur Luft und Raumfahrt (DLR) (Buckreuss et al., 2003), and the Constellation of Small Satellites for Mediterranean basin Observations (COSMO-SkyMed or CSK), developed by the Agenzia Spaziale Italiana (ASI) (Coletta et al., 2007). Three of these CSK satellites are already aloft, and the fourth will be launched within 2010. This technological scenario, destined to be further expanded, represents a great jump since the launch of the SIR-C/SAR-X mission in 1994, which provided the first X-SAR observations from space (e.g., Jameson et al., 1997).

In previous studies, we have developed theoretical and numerical models of the spaceborne X-SAR response to precipitation systems, characterized by liquid and frozen hydrometeor spatial distributions (Weinman and Marzano, 2008; Marzano and Weinman, 2008; Weinman et al., 2009; Marzano et al., 2009). There are still open issues related to further explore the potential of X-band high-resolution detection and retrieval of rainfall fields by exploiting X-SAR received signal co-polar amplitude and phase, and to evaluate the effects of spatial resolution degradation and inhomogeneous beam filling by precipitation. Near-surface rain rate can be retrieved from the

X-SAR backscatter coefficient using an empirically-based parametric regression technique, but both geometrical and volumetric effects need to be taken into account in a more effective way. Rainfall detection capability of X-SAR may be also tested using the repeat-pass coherence response to isolate the possible correlation degradation due to the precipitation field.

This paper is organized as follows. In Sect. 2 we will introduce: (i) TSX and CSK systems together with the basics of the X-SAR response interpretation; (ii) TMI and PR sensor specifications; (iii) weather radars used as ground "truth" data. In Sect. 3 two case studies will be analyzed and discussed. Within the TSX case study an improved empirically-tuned formula to retrieve rainfall rates from X-SAR signal attenuation will be presented. Repeat-pass coherence maps will be discussed to detect rainfall signature over land in central Italy. In Sect. 4 we will perform a quantitative analysis of atmospheric effects on spaceborne X-SAR rain rate estimation in terms of spatial resolution degradation and non-uniform beam filling. In Sect. 4, conclusions will be drawn.

2 Available space-based and ground-based data

Data sources and features will be briefly discussed together with the satellite-based and ground-based imagery available for the considered case studies.

2.1 X-SAR satellite data

The TerraSAR-X is an Earth observation satellite from DLR in partnership with EADS Astrium GmbH, designed to provide high-quality topographic information for commercial and scientific applications. The TerraSAR-X instrument is a 384-element active phased array X-band system with a centre frequency of 9.65 GHz (Buckreuss et al., 2003). The TSX satellite circles the Earth in a nearly polar orbit at approximately 514 km altitude with a flight speed of 7.6 km/s, and with a repetition rate of 11 days (due to electronic pointing agility, a 2.5-day revisit time can be achieved). Four modes of operations are foreseen, both at single polarization and at dual polarization, supporting both co-polar observations (HH, VV) and cross-polar ones (HV, VH), with an incident angle θ between 20° and 55°. The TSX acquires digital radar images, with resolution up to 1 m at the Earth's surface. When the target moves, such as precipitation (characterized by the advection of a turbulent flow of size-dependent falling particles), the X-SAR nominal resolution and geolocation could be significantly affected (Atlas and Moore, 1987), (Weinman et al., 2009). In typical rainfall situations the along-track resolution may degrade to ~135 m and the cross-track one to ~676 m.

The COSMO-SkyMed (COnstellation of small Satellites for the Mediterranean basin Observation) is an Earth observation satellite system, funded by the Italian Ministry of Research and Ministry of Defence and conducted by the Italian Space Agency (ASI), intended for both military and civilian use (Covello et al., 2010). The space segment of the CSK system includes four medium-sized satellites equipped with Synthetic Aperture Radar (SAR) sensors with global coverage of the planet. Observations of an area of interest will be repeated several times a day in all-weather conditions. The four satellites are planned for most sun-synchronous polar orbits, phased at 90° and at an altitude of 619 km with an orbit period of 97 min. The expected operating life of each satellite is estimated in 5 years. The first satellite COSMO-1 was launched at 22:34 GMT, on 8 June 2007, whereas COSMO-2 at 02:31:42 GMT on 9 December 2007 and COSMO-3 at 02:38 GMT on 25 October 2008, with COSMO-4 expected in 2010. Four modes of operations are foreseen with different resolution and coverage (i.e., Spotlight, Stripmap, Polarimetric, Scansar); those at single polarization supports both co-polar observations (HH, VV) and cross-polar ones (HV, VH), whereas the Polarimetric mode provides dual polarized radar returns. Incident angles θ is between 20° and 55° and spatial resolution goes from 100 m for the ScanSAR mode down to 1 m for the Spotlight mode.

2.2 TRMM satellite data

The Tropical Rainfall Measuring Mission (TRMM) is a joint mission between the USA National Aeronautics and Space Administration (NASA) and the Japanese National Space Development Agency (NASDA). The objectives of TRMM are to measure rainfall and energy (i.e., latent heat of condensation) exchange of tropical and subtropical regions of the world (Kummerow et al., 1998). The primary rainfall instruments on TRMM are the TRMM Microwave Imager (TMI), the Precipitation Radar (PR), and the Visible and Infrared Radiometer System (VIRS). The space segment of TRMM is a satellite in a 350-km circular orbit with a 35 ° inclination angle.

For our analysis we are mainly interested in the microwave instruments. The TMI is a nine-channel passive microwave radiometer at 10.65 GHz (Vertical V and horizontal H polarization), 19.35 GHz (V and H), 21.3 GHz (V), 37.0 GHz (V and H), 85.5 GHz (V and H) which grant a beam effective field-of-view (EFOV) of 63×37, 30×18, 23×18, 16×9 and $7\times5\,\mathrm{km}^2$, respectively. EFOV is the effective area swept by the antenna beam during the integration time. The PR is a radar consisting of a 128-element active phased array system operating at 13.8 GHz. Its swath width is 215 km, the horizontal resolution (at nadir) is 4.3 km and the range resolution is 0.25 km. It observes along the cross-track direction, within a scan angle of ±17°.

2.3 Ground-based weather radar

Due to their spatial and temporal coverage, operational ground-based Weather Radars (WRs) offer good opportunities to compare space-borne X-SAR imagery with precipitation ground-based measurements. Matching satellite and ground measurements is a difficult task due to spaceborne X-SAR frequency characteristics, the limited orbit duty-cycle, the relative small swath and the high spatial resolution.

The Next Generation Weather Radar (NEXRAD) network assures significant coverage of the whole USA with an acquisition time of the order of 5 min. This network is composed of Doppler radars designated Weather Surveillance Radar 1988 Doppler

(WSR-88D) (Fulton et al., 1998) which operates at S-Band horizontal polarization, and since mid 2008 it has been providing PPI data with a sample size of 250 m in range and 0.5° in azimuth ("Super-Resolution"). WSR-88D measurements are corrected for artifacts such as beam blockage, anomalous propagation and profile inhomogeneity, but residual errors may affect the estimated rainfall fields.

Data from the C-band Mt. Midia radar in central Italy have been also used (Picciotti et al., 2008). The Mt. Midia single-polarization weather radar is located at about 1700 m with an antenna beamwidth of 1.6° and a robust data quality control. Measurements are taken every 15 min with a spatial radial resolution of 250 m and azimuth angular resolution of 0.5°. Four elevation angles are usually acquired during an entire volume scan.

Rain rate R [mm/h] measurements are obtained from WR reflectivity Z mm^6/m^3 using a Z-R relation similar to Marshall-Palmer: the standard NEXRAD relation is $Z = 300\,R^{1.4}$ (Fulton et al., 1998), whereas for the Mt. Midia it is locally calibrated through rain-gauge networks (Picciotti et al., 2008). This kind of measurements may be subject to large systematic and random errors mainly due to the variability of drop size distributions which can be partially estimated only by using polarimetric radar systems (Marzano et al., 2008, and Ryzhkov et al., 2005), so that typical errors in the estimate of rainfall may exceed 50% (Fulton et al., 1998).

3 Case studies

With respect to a nadir-looking radar, the radar resolution volume of a side-looking radar, such as a SAR, is always represented by a slant slice of the atmosphere including the ground-range surface pixel. To model the X-SAR received Normalized Radar Cross Section (NRCS) in the presence of precipitation, we need to take into account both the two-way attenuation of surface NRCS due to rainfall and the atmospheric volume reflectivity. The NRCS for each cross-track pixel of the observed scene can be formally described by the sum of two terms (e.g., Weinman and Marzano, 2008):

$$\sigma_{\mathrm{SAR}}(x) = \sigma_{\mathrm{srf}}(x) + \sigma_{\mathrm{vol}}(x) \tag{1a}$$

with

$$\begin{cases} \sigma_{\mathrm{srf}}(x) = \sigma^0(x)\exp\left(-2\int_0^\infty k[x(z)]dz/\cos\theta\right) \\ \sigma_{\mathrm{vol}}(x) = \int_0^\infty \eta[x(z)]\exp\left(-2\int_z^\infty k\left[x'(z')\right]dz'/\cos\theta\right) \end{cases} \tag{1b}$$

where x is the cross-track ground coordinate, z the altitude, σ_{srf} is the co-polar backscattering NRCS from the surface, attenuated by the two-way path through the precipitating atmosphere, σ_{vol} is the volume co-polar backscattering NRCS, due to the ice, melted and liquid hydrometeor reflectivity weighted by the two-way path attenuation through the intervening precipitation, σ^0 is the surface backscattering coefficient, k is the co-polar specific attenuation, η the co-polar volumetric reflectivity, and θ is the incidence angle (with respect to the surface normal).

Two case studies are considered here, related to rainfall observations from TSX and CSK platforms. These case studies are introduced to show how X-SAR backscattering coefficient amplitude is suitable for rainfall content retrieval, whereas the use of the X-SAR interferometric phase may be exploited for precipitation detection.

3.1 Hurricane "Gustav" observed from TSX, TRMM and WR

For our analysis we have considered a case study over Mississippi centered at about 30.5° N × 89.5° W, acquired by TerraSAR-X on 2 September 2008 12:00 UTC (from 11:58:44 to 11:59:06 UTC). The same scene was observed by the ground-based NEXRAD weather radar (WR), located in Mobile (AL) with a time difference of about 1 min (acquisition started at 11:59:44 UTC). For this case study, no TSX "background image" was available to show the same scene without rainfall in order to better separate the contribution of the surface background. The selected area was observed by TRMM at about 15:30 UTC; from the radio-sounding performed in Birmingham (AL) at

12:00 UTC, we have estimated that the freezing level height was about 4.5 km. The selected case study refers to the passage of Hurricane "Gustav" over Louisiana and Mississippi northwestward, moving at an average velocity of 24 km/h, delivering torrential rains to the central gulf coast of the USA (e.g. Larto Lake, LA, reported a rainfall total accumulation of 533.4 mm).

TSX data were available in ScanSAR horizontally-polarized mode and obtained as Level-1b Multi-look Ground Detected (MGD) format (Buckreuss et al., 2003). The MGD format presents a reduced speckle, due to the six-looking averaging, and is obtained by a simple polynomial slant-to-ground projection in range using WGS84 ellipsoid and an average constant terrain height; the choice to avoid automatic terrain corrections reduces the circumstance of removing rainfall signatures being the latter potentially confused with topographic effects. The resolution of TSX ScanSAR image on ground is about $18 \times 18\,\mathrm{m}^2$. TSX data have been calibrated using the annotation and geo-location data set provided with the TerraSAR-X Level-1b package. Colocated NEXRAD WR data were available in terms of Level-II horizontally-polarized radar reflectivity factor Z with a spatial resolution of about 0.25 km in range and 0.5° in azimuth and nominal coverage radius of about 209 km.

A pre-processing procedure is necessary to compare TSX and WR data, due to differences in their spatial coverage and resolution. Both images have been co-registered and degraded through an appropriate moving-average filter at the resolution of about 500 m and down-sampled at about 500 m. Spatial features are consistent with the effective resolution obtainable from X-SAR processing techniques applied to incoherent moving targets, such as precipitation (e.g., Marzano et al., 2010). Finally, TSX and WR have been projected adopting an Universal Transverse Mercator (UTM) coordinate system.

The considered case study was first analyzed in Marzano et al. (2010). In the latter paper, a regressive empirical algorithm (REA) for X-SAR rainfall retrieval was applied, having the following power-law expression:

$$\hat{R}_{\mathrm{REA}}(x) = a_e \left[\sigma^0_{\mathrm{dB}}(x) - \sigma_{\mathrm{SARdB}}(x)\right]^{b_e} = a_e \Delta\sigma^{b_e}_{\mathrm{SARdB}}(x) \tag{2}$$

where x is a point on the cross-track direction, σ^0_{dB} (dB) is the background NRCS, σ_{SARdB} (dB) is the TSX retrieved NRCS such that $\Delta\sigma_{\mathrm{SARdB}} = \sigma^0_{\mathrm{dB}} - \sigma_{\mathrm{SARdB}}$ is positively defined. The criterion $\Delta\sigma_{\mathrm{SARdB}} > 0$ is assumed to be a rain detection rule and its accuracy strongly depends on the knowledge of background σ^0_{dB}. In Eq. (3) R_{REA} is the estimated rain rate (mm/h); a_e and b_e are two empirical parameters that we have determined to be respectively 3.37 and 1.55 supposing an average background σ^0_{dB} equal to −7.9 (dB), obtained from the mean of the surrounding non-raining pixels in the same X-SAR image with a standard deviation of about 1 dB (Marzano et al., 2010).

The X-SAR side-viewing geometry introduces a characteristic pattern of the observed NRCS due to the increasing attenuation path as the incident radar ray moves within the precipitation cell from near to far ranges (e.g., Weinman and Marzano, 2008). This deformation is such that the X-SAR tends to underestimate rainfall intensity at the near-range edges and to overestimate it at the far-range edges with a fictitious broadening of the rainfall footprint. In order to take these geometrical effects into account, we have modified the retrieval formula Eq. (3) by introducing a factor $f_G(x)$ that accounts for the location of a pixel with respect to the edge cell. Moreover, for heavy rainfall intensity the model of Eq. (3) tends to underestimate the volumetric backscattering contribution σ_{vol}, as in Eq.(1); this effect may be partially corrected by a first-order approach. The new formulation of the X-SAR modified regressive empirical algorithm (MREA), briefly derived in the Appendix, becomes:

$$\hat{R}_{\mathrm{MREA}}(x) = \begin{cases} \left[\dfrac{\Delta\sigma_{\mathrm{SARdB}}(x) + b_v \Delta\sigma^{c_v}_{\mathrm{SARdB}}(x)}{a}\right]^{1/b} \left[\dfrac{1}{(x-x_0)}\right]^{c_e} & x_0 + \varepsilon \le x \le x_0 + w \\ 0 & \text{otherwise} \end{cases} \tag{3}$$

where the parameters a, b, b_v, c_v and c_e are regressive coefficients, obtained by least-square regression analysis and estimated to be, respectively, 0.0089, 2.4595, 0.1216, 3.8979 and −0.0230. The parameter ε in Eq. (4) is introduced to prevent the singularity in $x = x_0$ and is usually equal to few pixels in the ground range. The previous Eq. (4) applies to all the TSX pixels where $\Delta\sigma_{\text{SARdB}} \geq 1$ taking into account the σ^0_{dB} background uncertainty. The parameter x_0 is the near-range edge of the rain cloud with w its cross-track width, derived from measured NRCS cross-track curve such that $\Delta\sigma_{\text{SAR}}$ intersects the threshold value. Note that in order to empirically tune Eq. (4) with ground reference, WR rain rate estimates have been obtained by inverting the Z-R relation:

$$\hat{R}_{\text{WR}}(x) = \left[Z(x)/a_r\right]^{b_r} \tag{4}$$

where Z is the measured reflectivity factor (mm^{6}m^{-3}), R_{WR} is the estimated rain rate (mm/h), $a_r = 300$ and $b_r = 1.4$, in case of a NEXRAD standard relation (note that in Marzano et al., 2010, the Marshall-Palmer Z-R was used instead).

3.2 Orographic precipitation observed from CSK and WR

A case study in Central Italy has been selected by accessing to the archive of Mt. Midia C-band WR data (Picciotti et al., 2008). The covered area is affected by both western and eastern fronts coming from the Atlantic Ocean and Siberia, respectively. Orographic precipitation plays a crucial role due to the Appennine range (up to nearly 3000 m). Mesoscale Convective Systems (MCS) may develop within the area with cluster organized cells during late summer and early fall, very often causing localized hailstorms.

Whilst in the previous case study we have concentrated on the analysis of the backscattering amplitude coefficient, in this case we have exploited the CSK multiplatform constellation to evaluate the temporal interferometric response of X-SAR measurements to rainfall areas. It is well known in literature that the atmosphere produces phase delay on the SAR signal, which is composed by two main contributes, ionospheric and tropospheric (e.g., Quegan and Lamont, 1986). The refractivity of air introduces uncertainties in the time of arrival of the microwave signal due to the bending and slowing along the propagation path. The ionospheric effect is inversely proportional to the square of the radar frequency in the microwave part of the spectrum, so that lower frequencies could be more affected by the path delay, particularly near the geomagnetic equator and poles (Massonnet and Feigl, 1998). Conversely, at microwave frequencies the tropospheric unpredictable effect on path delay is essentially due to water vapor content and cloud hydrometeors, the former being spectrally non-dispersive, whereas the latter is strongly frequency-dependent (and fairly significant at frequencies above C band). The phase delay in the clear troposphere consists of hydrostatic and wet components. Although the latter is smaller in magnitude (about 30 cm on average at frequencies less than 10 GHz), it is far more spatially variable than the hydrostatic and ionospheric delays. In fact, changes in the distribution of water vapor are associated with clouds, convection, and storms. In addition, variations resulting from orographic, frontal, coastal, and seasonal gradients may be present.

In the presence of hydrometeors (such as fog, rain, hail, snow, and graupel) there is a contribution to the path delay. Sohleim et al. (1999) computed path delays induced by rain, hail and snow at the Global Positioning System (GPS) carrier frequencies, obtaining a path delay of about 6 mm for light rain of 20 mm/h (delay of 2 mm/km for a nadir rain scale height of 3 km) up to 9 cm for heavy rain of 200 $\text{mm}\cdot\text{h}^{-1}$ (delay of 15 mm/km at L2 carrier for a rain scale height of 6 km). Based on analysis of two X-SAR interferograms, Moissev and Hanssen (2003) showed that precipitation caused an enhanced signal delay, but the most probable explanation of this effect was an increase in water vapor concentration due to partial evaporation of raindrops. Simulations at C band and X band show that for 100 mm/h and 5 km nadir rain- scale height the two-way range delay may be about 5 cm, whereas for 10 mm/h and 5 km nadir rain path the two-way range delay is about 1 cm (Matricciani, 2009). Finally, if the hydrometeor concentration is such to produce a fluctuation of the refractive index, the latter could cause a random phase error in the SAR signal, affecting the signal coherence (Quegan and Lamont, 1986). Stemming from the above mentioned issues, the X-band SAR data from COSMO-SkyMed mission and the interferometric coherence seem to be a way for detecting rain from a high resolution spaceborne radar imagery.

Concerning the raining event occurred on 18 May 2009 in a region close to L'Aquila city (Italy), four COSMO-SkyMed images, acquired on four different days, have been used. The acquisition dates are: 10 May 2009, 11 May 2009, 18 May 2009 and 27 May 2009, so that, among these data, only one concerns the precipitation event. The images are right descending, with a mean incidence angle of 36°. They belong to the same satellite track, thus being useful for interferometric purposes, and have a geometric resolution of 2.2 m (both in slant range and azimuth).

The interferometric X-SAR complex coherence ρ_{coh} feature between couples of X-SAR images has been exploited in order to investigate whether this kind of precipitation event could be detected by X-band SAR data. The complex coherence (or correlation) ρ_{coh} is defined as (e.g., Burgmann et al., 2000):

$$\rho_{\text{coh}}(x,y) = \frac{< s_1(x,y)s_2^*(x,y) >}{\sqrt{< s_1(x,y)s_1^*(x,y) >< s_2(x,y)s_2^*(x,y) >}} \tag{5}$$

where s_1 and s_2 are the corresponding complex pixel values, and the angle brackets indicate the expected value at the pixel of coordinates (x,y), estimated by spatial averaging. The coherence ρ_{coh} is mostly influenced by the phase difference between radar returns, a distinctive parameter measured by a coherent sensor, and is particularly related to the spatial arrangement of the scatterers within the pixel and thus to their possible displacements.

Zebker and Villasenor (1992) stated that the three main sources of SAR decorrelation are: spatial decorrelation (mostly related to the perpendicular baseline between acquisitions), thermal decorrelation and temporal decorrelation, which accounts for physical changes over the time period between two acquisitions. The temporal term is the subject we want to investigate in order to understand if the rain event causes changes in the interferometric coherence. Since it is not possible to estimate exactly the spatial and the thermal decorrelation, we can compute more than one interferogram trying to keep constant the contribution of the first two terms (spatial: same perpendicular baseline; thermal: same antenna). In this way it is possible to single out the temporal term by performing comparisons between the interferograms. Following this idea, three interferograms, which have perpendicular baselines spanning from 160 to 180 m, have been computed, using the following couples of images: 10–11 May, 10–27 May and 11–18 May. Only the last interferogram includes the rain event.

The interferograms have been computed with a spatial resolution of about ~23 m, since a 10 × 10 multi-look processing was applied, in order to enhance the signal-to-noise ratio. After the topographic-phase removal, the coherence feature has been computed for each interferogram, using 5 × 5 pixels windows (~ 115 × 115). The three geocoded phase coherence images, with a geometrical resolution of 130 × 130 m^2, are shown in Fig. 6a in an RGB color composition: 10–11 May 2009 (Red, hereafter cc_{10-11}), 10–27 May 2009 (Green, hereafter cc_{10-27}) and 11–18 May 2009 (Blue, hereafter cc_{11-18}). It is possible to see a yellow area (Red and Green are higher than Blue, i.e., the phase coherence is larger for the couples without rain), which is probably the area affected by rain on 18 May. In Fig. 6b it is also shown the precipitation map of the same area as observed by the C-band Mt. Midia weather radar in terms of reflectivity factor Z. Note the maximum Z of about 45 dBZ, much less than the values up to 59 dBZ observed during the hurricane "Gustav" in Fig. 1.

As expected, the cc_{10-11} has an higher value, almost anywhere, with respect to cc_{10-27} and cc_{11-18}, because it has only one day of temporal baseline. It is interesting to note that, in the region where we suppose the presence of rain effects (the red region in Fig. 6c; Red = cc_{10-27}, Green = Blue = cc_{11-18}), cc_{10-27} has coherence values higher with respect to those of cc_{11-18} including the rain event, despite the difference between the temporal baselines (ten days).

It is worth noting that the possible rain effect in Fig. 6a is eastward with respect to the detected rain in Fig. 6b, because of the geometric acquisition of the SAR satellite, which is right looking, descending orbit, with a looking angle of 36° with respect to the vertical. The shift of the rain pattern is therefore perfectly coherent with the consideration that the pixels mostly affected by the rain event are those encountering more rain in the sensor-target path.

4 Spatial variability of rainfall fields observed from space

The potential of X-SAR high-resolution rain field retrieval may be qualitatively appreciated by spatially degrading TSX imagery taking into account the antenna pattern effect of the resolution-degraded sensor. Examples of inhomogeneous rain beam-filling can be also analyzed in terms of spatial variability of the rain fields.

4.1 Effect of spatial-resolution degradation

In order to perform the analysis of spatial resolution impact, we have developed an *ad hoc* numerical simulator. The algorithm receives an input map, at a known spatial resolution, and down-samples it to an output map at a desired resolution. The output macro-pixel values are obtained by applying a spatial filter to all the input pixel values corresponding to the same output macro-pixel. The filter may be either a rectangular moving average or a Gaussian form with a box width or a standard deviation, respectively, related to the half-power beamwidth of the sensor field-of-view (FOV). We have applied this numerical simulator to TSX data to simulate what TRMM-PR and TRMM-TMI would have observed if those sensors had replaced the TSX antenna: we have indicated these synthetic images as TSX-PR and TSX-TMI products.

As already mentioned, the considered linear resolution for TSX and WR is 0.5 km, whereas that of TSX-PR is 4 km and that of TSX-TMI is 15 km, the latter being considered as an approximation of the resolution of TMI channel at 37 GHz, and selected as example of low-resolution data. Note that the subsequent discussion only regards the geometric consequences due to reduced resolution and antenna pattern, whereas the effects due to frequency-band difference are not considered (e.g., Marzano et al., 2002).

These effects can be justified by noting that the sensor antenna spatial integration tends to weaken rain peaks. The importance of the latter effect is clearly observable from TSX-TMI map in Fig. 7, where the rain-field smoothing is so strong that some WR-observed precipitation patterns are nearly diluted around zero.

The correlation of rainfall estimates between WR and TSX, TSX-PR, TSX-TMI can be analyzed with some more details. WR data have been processed by down-sampling the rain-estimated image by a factor of 8 and 30, respectively, to yield TSX-PR and TSX-TMI results. In case of TSX-PR spatial degradation, the correlation is 0.54, the error bias is equal to 6.41 mm/h, the RMSEs are equal to about 36.78 mm/h and the FRMSE is equal to 1.62. In case of TSX-TMI spatial degradation, the correlation is of 0.09, the error biases is equal to −1.40 mm/h, the RMSEs is equal to about 17.48 mm/h and the FRMSE is equal to 0.77. These numbers must be compared with those obtained at TSX resolution, where the correlation is of 0.75, the error bias is equal to −0.66 mm/h, the RMSE is equal to about 22.28 mm/h and the FRMSE is equal to 0.98.

4.2 Effects of non-uniform beam filling

Beam filling is the systematic error introduced when the field-of-view (FOV) of the spaceborne sensor is not filled with uniform rain and can lead to significant underestimation of rain rates (Kummerow, 1998). We can estimate the consequence of inhomogeneous beam filling on TSX-PR and TSX-TMI by choosing two sample pixels, the first one centered at about 31.38° N × 89.33° W, and the second one centered at about 31.00° N × 89.96° W. The first region is around the rain rate peak of the rainfall map and it emphasizes the spatial degradation introduced on spatial resolution. The second pixel, on the other hand, is a region corresponding to low rain rates within the Hurricane "Gustav" rain-band.

For the two regions we have derived the occurrence histogram of WR rain rate within the pixel area, grouping the pixel by means of the down-sampling factor. The obtained results are shown in Figs. 8 and 9. In these figures both PR-like and TMI-like are shown; all plots present a red bar corresponding to the TSX-PR or TSX-TMI value for the selected pixel.

Figure 8 is relative to the rain peak area. The rain-rate for TSX-PR ranges from 70.71 to 282.61 mm/h, whereas for TSX-TMI from 4.99 to 292.79 mm/h. Within the macro-pixel area, the rain rate variability is fairly high and for TSX-TMI most values are relative to non-rain points with low values. This means that low-resolution spaceborne sensors cannot follow the observed precipitation spatial variability and may introduce significant estimation errors with respect to the WR "ground truth": in our case we have an error maximum (in absolute value) of 170.97 mm/h for TSX-PR and 244.21 mm/h for TSX-TMI. Satellite-based rainfall algorithm validation by rain gauges becomes problematic in such conditions, due to the punctual nature of gauge measurements. Another effect is due to sensor-antenna pattern: the retrieved rain rate from TSX-PR (111.64 mm/h) and TSX-TMI (48.58 mm/h) are lower than the simple mean of WR values (respectively 176.66 mm/h and 148.89 mm/h), because of the weighting (Gaussian) introduced by the antenna pattern.

The same conclusions can be derived by Fig. 9 relative to the low rain-rate area: the range of rain-rate values for TSX-PR is from 1.23 mm/h to 16.35 mm/h; for TSX-TMI the range of rain-rate values is from 0.63 mm/h to 35.54 mm/h. The maximum error (in absolute value) is 10.48 mm/h for TSX-PR and 24.64 mm/h for TSX-TMI. The retrieved rain rate from TSX-PR is 11.71 mm/h and from TSX-TMI is 10.90 mm/h while the simple mean of WR values is, respectively, 8.79 mm/h and 18.09 mm/h.

The effect of the antenna pattern filtering is also shown in Figs. 8 and 9. Their bottom panels show the occurrence histogram of WR rain rates within the pixel area after the Gaussian filtering which emulate the antenna pattern; pixel are grouped by a down-sampling factor. In these plots the red line represents the central pixel value. In Fig. 8 we can observe a compression of WR rain rate with respect to top-panel figures, where the Gaussian filtering is not present, and the pixel value is nearer to the WR most probable value, represented by the histogram peak. However, the "observed" rain rate distribution is very different from the "real" one: this is particularly evident on the TSX-TMI histogram where all the non-rain points have almost disappeared. For the bottom panel of Fig. 9 the conclusions are different: for TSX-PR it yields a compression of

WR data with values are larger than WR "observed" values, whereas there is not such compression for TSX-TM with values again larger than most WR rain rate values. It is worth stressing that these results have been obtained by a sensor simulator where a Gaussian filter has been applied to the pixel area without considering the antenna side-lobe effects.

5 Conclusions

The new generation of spaceborne X-SARs that operate nowadays may provide important opportunities to measure rainfall over land with spatial resolution between a few hundreds of meters and 1 km, even though several issues must still be addressed. An analysis of two case studies, related to Hurricane "Gustav" on 2008 over Mississippi using co-registered WR and TSX X-SAR data and nearly contemporary TRMM ones, and to a Central Italy storm event observed by CSK in 2009, has shown: (i) a correlation between WR reflectivity measurements and X-SAR measured NRCS; (ii) a correlation between the X-SAR temporal coherence reduction and WR reflectivity field. Since SAR side-looking observation of precipitation tends to introduce a geometrical deformation of the retrieved field, we have also suggested a modified regressive empirical model to estimate rainfall rate from X-SAR whose comparison with WR estimates provides a RMSE less than 25 mm/h for hurricane torrential rainfall. Using numerical spatial filters to simulate the resolution of TRMM-PR and TRMM-TMI, it has been evaluated how spatial resolution affects in a significant way not only the covered area (providing an attribution error), but also the retrieved measurements and the sensitivity to lower rain rates, which are almost lost at lower resolutions.

The presented results are encouraging, even though more quantitative analyses are necessary regarding the effects of spatial resolution degradation and inhomogeneous beam filling of precipitation fields on physical hydrologic analyses. The suggested X-SAR rainfall retrieval algorithms need a systematic calibration and validation using several case studies. Further developments are foreseen toward more sophisticated inversion methodologies, whereas better comprehension of spaceborne observed precipitations can arise from the use of mesoscale cloud models coupled with SAR response model and from the polarimetric capability of spaceborne X-SARs and ground-based WR sensors. The proposed technique of X-SAR rainfall algorithm calibration uses Weather Radar measurements. An appealing idea is to design a synergetic approach between X-SAR and geostationary weather satellites with the purpose to develop a fully spaceborne framework for X-SAR Earth observations. These issues need to be still investigated and will be the objective of future works.

Appendix A

Derivation of X-SAR modified regressive empirical algorithm

The retrieved heavy rainfall, using the REA inversion formula given by Eq. (3), usually appears to be underestimated when applied to X-SAR data (see Marzano et al., 2010). Indeed, we may not be able to ignore the volume contribution to σ_{SAR} within heavy rainfall as well as the geometric deformation of X-SAR slant-view observation. Suppose that we can assume to have an infinitely wide rain cloud where the X-SAR NRCS is given by (e.g., Weinman and Marzano, 2008):

$$\sigma_{\mathrm{SAR}} = \sigma^0 e^{-2k(z_0/\cos\theta)} + \frac{\eta\cos\theta}{2k}\left[1 - e^{-2k(z_0/\cos\theta)}\right] \qquad \text{(A1)}$$

where k is specific attenuation, η is the volumetric reflectivity, z_0 is freezing level, θ the incident angle. We can rewrite Eq. (A1) as:

$$\sigma_{\mathrm{SAR}} = \sigma^0 e^{-2k(z_0/\cos\theta)}\left[1 + \frac{\eta\cos\theta}{2k\sigma^0}\left(e^{2k(z_0/\cos\theta)} - 1\right)\right] \qquad \text{(A2)}$$

Taking the natural logarithm of Eq. (A2), we get:

$$\ln\sigma_{\mathrm{SAR}} = \ln\sigma^0 - 2k\left(z_0/\cos\theta\right) + \ln\left[1 + \frac{\eta\cos\theta}{2k\sigma^0}\left(e^{2k(z_0/\cos\theta)} - 1\right)\right] \qquad \text{(A3)}$$

By also defining:

$$\Delta\sigma_{\mathrm{SAR}} = \ln\sigma^0 - \ln\sigma_{\mathrm{SAR}} = \Delta\sigma_{\mathrm{SAR}dB}/4.343 \tag{A4}$$

and approximating:

$$\ln\left[1 + \frac{\eta\cos\theta}{2k\sigma^0}\left(e^{2k(z_0/\cos\theta)} - 1\right)\right] \approx \frac{\eta z_0}{\sigma^0} \tag{A5}$$

we obtain:

$$\Delta\sigma_{\mathrm{SAR}} = 2kz_0/\cos\theta - \eta z_0/\sigma^0 \tag{A6}$$

By posing $k = aR^b$ and $\eta = cR^d$ (Weinman and Marzano, 2008), we can write:

$$\Delta\sigma_{\mathrm{SAR}} = AR^b - BR^d \tag{A7}$$

where A and B are two proper coefficients, derived from Eq. (A6) or from empirical least-square analysis. The previous equation can be further approximated at first-order by using Eq. (3) into the volumetric term to yield:

$$\Delta\sigma_{\mathrm{SAR}} \cong AR^b - B[a_e(4.343\Delta\sigma_{\mathrm{SAR}})^{b_e}]^d \tag{A8}$$

By inverting Eq. (A8), the rainfall inversion model may be expressed by:

$$\hat{R} \cong \left[\frac{\Delta\sigma^{+}_{\mathrm{SAR}} B[a_e(4.343\Delta\sigma_{\mathrm{SAR}})^{b_e}]^d}{A}\right]^{1/b} \tag{A9}$$

Note that setting $B = 0$ in Eq. (A9) gives a form that is the same as Eq. (3), but including the second term increases the large R values for a given $\Delta\sigma_{\mathrm{SAR}}$. Finally, in order to mitigate the geometrical error due to the X-SAR cross-track slant view, we can introduce an empirical geometrical factor f_G, expressed by:

$$f_G(x) = \begin{cases} \left[1/(x-x_0)\right]^{c_e} & x_0+\varepsilon \le x \le x_0+w \\ 0 & \text{otherwise} \end{cases} \tag{A10}$$

where w is the cross-track cell width (km) and x_0 the point where the incident SAR ray begins to intersect the cell (see Marzano and Weinman, 2008; Marzano et al., 2010). The small increment ε in Eq. (A10) is introduced to prevent the geometrical factor $f_G(x)$ in Eq. (A10) from becoming infinite. This means that the final modified regressive empirical algorithm (MREA) can be rearranged as follows:

$$\hat{R}_{\mathrm{MREA}}(x) = \left[\frac{\Delta\sigma_{\mathrm{SARdB}}(x) + b_v \Delta\sigma^{c_v}_{\mathrm{SARdB}}(x)}{a}\right]^{1/b} f_G(x) \tag{A11}$$

where the parameters a, b, b_v, c_v and c_e are unknown coefficients to be derived from an empirical regression analysis. The Eq. (A11) justifies the retrieval statistical parametric model, proposed in Eq. (4).

Acknowledgements. The authors would like to thank E. Picciotti (Italy), A. Roth and S. Lehner (DLR, Germany) for their cooperation and the helpful discussions. We also acknowledge the TSX Science Team for providing the TSX MGD data under the "AtmoX" project and the CSK Science Team for providing CSK data under the "RainXSAR" project. NCDC-NOAA is gratefully acknowledged for providing NEXRAD weather radar data and software tools (www.ncdc.noaa.gov/oa/wct), NASA GES-DISC, US for providing TRMM data and tools (disc.sci.gsfc.nasa.gov), Regione Abruzzo (Italy) for providing C-band Mt. Midia radar data. This work has been partially supported by the National Department of Civil Protection, Rome (Italy) and by Region Abruzzo (Italy).

References

Atlas, D. and Moore, R. K.: The measurement of precipitation with synthetic aperture radar, J. Atmos. Ocean. Tech., 4, 368–376, 1987.

Bennartz, R. and Petty, G. W.: The sensitivity of microwave remote sensing observations of precipitation to ice particle size distributions, J. Appl. Meteorol., 40, 345–364, 2001.

Buckreuss, S., Balzer, W., Muhlbauer, P., Werninghaus, R., and Pitz, W.: The TerraSAR-X satellite project, in Proc. IGARSS, 5, 3096–3098, 2003.

Burgmann R., Rosen, P. A., and Fielding, E. J.: Synthetic aperture radar interferometry to measure Earth's surface topography and its deformation, Annu. Rev. Earth Planet. Sci., 28, 169–209, 2000.

Chandrasekar, V. and Fritz, J.: Simultaneous observations of X-band polarimetric SAR and ground-based weather radar during a tropical storm to characterise the propagation effects, in Proc. EUCAP, Berlin, Germany, March 23–27, 2009.

Coletta, A., Angino, G., Battazza, F., Caltagirone, F., Impagnatiello, F., Valentini, G., Capuzi, A., Fagioli, S., and Leonardi, R.: COSMO-SkyMed program: Utilization and description of an advanced space EO dual-use asset, in Proc. Envisat Symp., Montreux, Switzerland, April 23–27, 2007. (ESA SP-636), 2007.

Covello, F., Battazza, F., Coletta, A., Lopinto, E., Fiorentino, C., Pietranera, L., Valentini, G., and Zoffoli, S.: COSMO-SkyMed an existing opportunity for observing the Earth, J. Geodyn., 49, 171–180, 2010.

Danklmayer, A., Doring, B. J., Schwerdt, M., and Chandra, M.: Assessment of Atmospheric PropagationEffects in SAR Images", IEEE T. Geosci. Remote Sens., 47, 112–132, 2009.

Dingman, S. L.: Physical Hydrology, 2nd Edition Prentice-Hall, Inc., 113 Sylvan Ave. Englewood Cliffs NJ, USA, 656 pp., 2002.

Durden, S. L., Haddad, Z. S., Kitiyakara, A., and Li, F. K.: Effects of non-uniform beam filling on rainfall retrieval for the TRMM Precipitation Radar, J. Atmos. Ocean. Tech., 15, 635–646, 1998.

Fulton, R. A, Breidenbach, J. P., Seo, D.-Jun, Miller, D. A., and O'Bannon, T.: The WSR-88d Rainfall Algorithm, Weather Forecast., 13, 377–395, 1998.

Jameson, A. R., Li, F., Durden, S. L., Haddad, Z. S., Holt, B., Fogary, T., Im, E., and Moore, R. K.: "SIR-C/X-SAR observations of rainstorms", Remote Sens. Environ, 59, 267–279, 1997.

Kummerow, C., Barnes, W., Kozu, T., Shiue, J., and Simpson, J.: The Tropical Rainfall

Measuring Mission (TRMM) Sensor Package, J. Atmos. Ocean. Tech., 15, 809–817, 1998.

Iguchi, T., Kozu, T., Meneghini, R., Awaka, J., and Okamoto, K.: Rain profiling algorithm for the TRMM Precipitation Radar, J. Appl. Meteorol., 39, 2038–2052, 2000.

Melsheimer C., Gade, M., and Alpers, W.: Investigation of multifrequency/ multipolarization radar signatures of rain cells derived from SIR-C/X-SAR data, J. Geophys. Res., 103, 18867–18884, 1998.

Marzano F.S., Mugnai, A., and Turk, F. J.: Precipitation retrieval from spaceborne microwave radiometers and combined sensors, in: Remote Sensing of Atmosphere and Ocean From Space: Models, Instruments and Techniques, edited by: Marzano F. S. and Visconti, G., Dordrecht, The Netherlands, Kluwer, 107–126, 2002.

Marzano, F. S., Scaranari, D., Vulpiani G., and Montopoli, M.: Supervised classification and estimation of hydrometeors using C-band dual-polarized radars: a Bayesian approach, IEEE T. Geosci. Remote Sens., 46, 85–98, 2008.

Marzano, F. S. and Weinman, J. A.: Inversion of spaceborne X-band synthetic aperture radar measurements for precipitation remote sensing over land, IEEE T. Geosci. Remote Sens., 46, 3472–3487, 2008.

Marzano, F. S., Mori, S., Pierdicca, N., Pulvirenti, L., and Weinman, J. A.: Characterization of atmospheric precipitation effects on spaceborne synthetic aperture radar response at X, Ku, Ka band, Ital. J. Remote Sens., 41, 73–88, 2009.

Marzano, F. S., Mori, S., and Weinman, J. A:, Evidence of Rainfall Signatures on X-Band Synthetic Aperture Radar Imagery Over Land, IEEE Trans. Geosci. Remote Sens., 48, 950–964, 2010.

Massonnet D. and Feigl, K. L.: Radar interferometry and its application to changes in the Earth's surface, Rev. Geophys., 36, 441–500, 1998.

Masunaga, H., Satoh, M., and Miura, H.: A joint satellite and global cloud-resolving model analysis of a Madden–Julian Oscillation event: Model diagnosis, J. Geophys. Res., 113, D17210, doi:10.1029/2008JD009986, 2008.

Matricciani, E: A Relationship Between Phase Delay and Attenuation Due to Rain and Its Applications to Satellite and Deep-Space Tracking, IEEE T. Antenn. Propag., 57, 3602–3611, 2009.

Moisseev, D. and Hanssen, R.: Influence of hydrometeors on InSAR observations, Proc. of Geoscience and Remote Sensing Symposium, IGARSS 2003, IEEE International, 6, 21–25, 3811–3814, July 2003.

Picciotti E., Gallese B., Cimoroni A., Montopoli M., Telleschi A., Volpi A., Consalvi F., and Marzano F. S.: C-band radar precipitation measurements in mountainous region: comparison with raingauge fields and X-band radar data, Proceeding of the 5th “European conference on radar in meteorology and hydrology ERAD 2008“, 2008.

Quegan S. and Lamont, J.: Ionospheric and tropospheric effects on synthetic aperture radar performance, Int. J. Remote Sens., 7, 525–539, 1986.

Ryzhkov, A., Giangrande, S. E., and Schuur, T. J.: Rainfall estimation with a polarimetric prototype of WSR-88D, J. Appl. Meteorol., 44, 502–515, 2005.

Solheim, F. S., Vivekanandan, J., Ware, R. H. and Rocken, C.: Propagation delays induced in GPS signals by dry air, water vapor, hydrometeors, and other particulates, J. Geophys. Res. Atmos., 104 (D8), 9663–9670, 1999.

Tapiador, F. J., Kidd, C., Levizzani, V., and Marzano, F. S.: A neural networks-based PMW-IR fusion technique to derive half hourly rainfall estimates at 0.1° resolution, J. Appl. Meteorol., 43, 576–594, 2004.

Weinman, J. A. and Marzano, F. S.: An exploratory study to derive rainfall over land from spaceborne synthetic aperture radars, J. Appl. Meteor. Climatol., 47, 562–575, 2008.

Weinman, J. A., Marzano, F. S., Plant, W. J., Mugnai, A., and Pierdicca, N.: Rainfall observation from X-band, space-borne, synthetic aperture radar, Nat. Hazards Earth Syst. Sci., 9, 77–84, doi:10.5194/nhess-9-77-2009, 2009.

Zebker, H. A. and Villasenor, J.: Decorrelation in interferometric radar echoes, IEEE T. Geosci. Remote Sens., 30, 950–959, 1992.

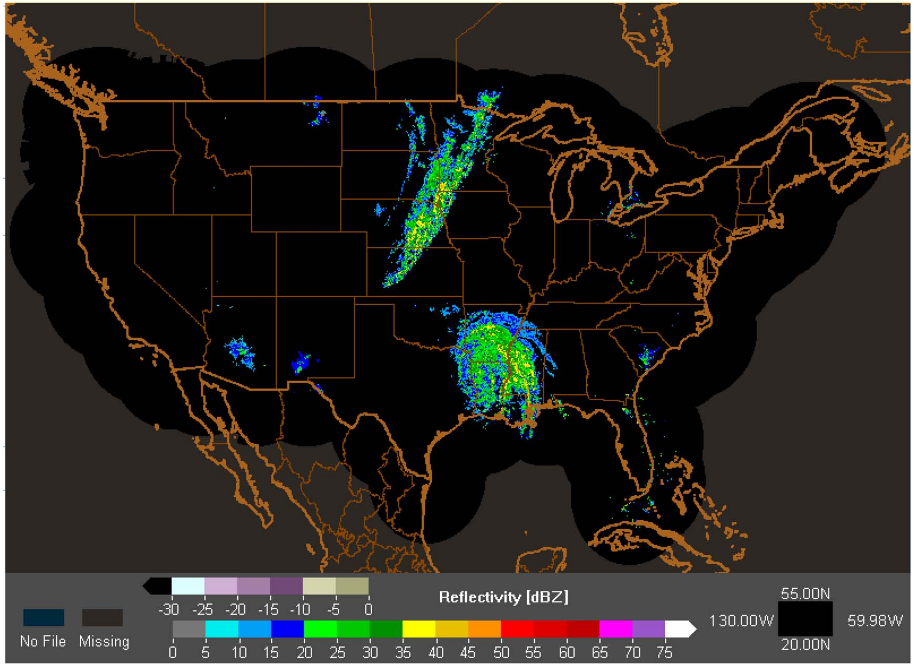

Fig. 1. NEXRAD National Radar Reflectivity mosaic (in dBZ) on 2 September 2008 at 12:00 UTC. We can observe the signature of Hurricane "Gustav" covering Louisiana, Mississippi and Arkansas.

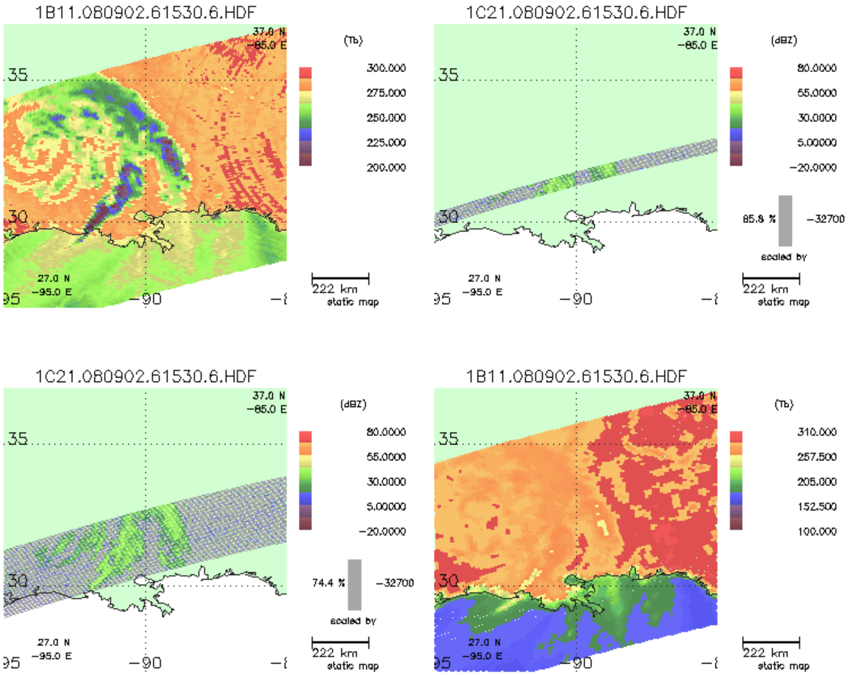

Fig. 2. TRMM observations over the selected case study of Louisiana and Mississippi, 2 September 2008 at 15:30 UTC. (Top panels) TRMM 1B11 brightness temperature (TB) product relative to TMI channel 7 (37 GHz horizontal polarization, left), beam effective field-of-view (EFOV) of 16 × 9 km^2, and TMI channel 9 (85.5 GHz horizontal polarization, right) with a main-beam EFOV of 7 × 5 km^2. The convective cell indicated in Fig. 1 is near-fully imaged. (Bottom panels) The TRMM 1C21 radar reflectivity (dBZ) product, relative to PR normal sample (left) range bin 75, and PR rain oversample (right), range bin 16. Note that the PR swath is 220 km wide (reduced in the oversampled product) and the range resolution is 0.25 km; TMI swath is 760 km wide. This image has been realized by using NASA/GSFC PPS Orbit Viewer.

Title Page
Abstract
Introduction
Conclusions
References
Tables
Figures
◀▌ ▌▶
◀ ▶
Back
Close
Full Screen / Esc
Printer-friendly Version
Interactive Discussion

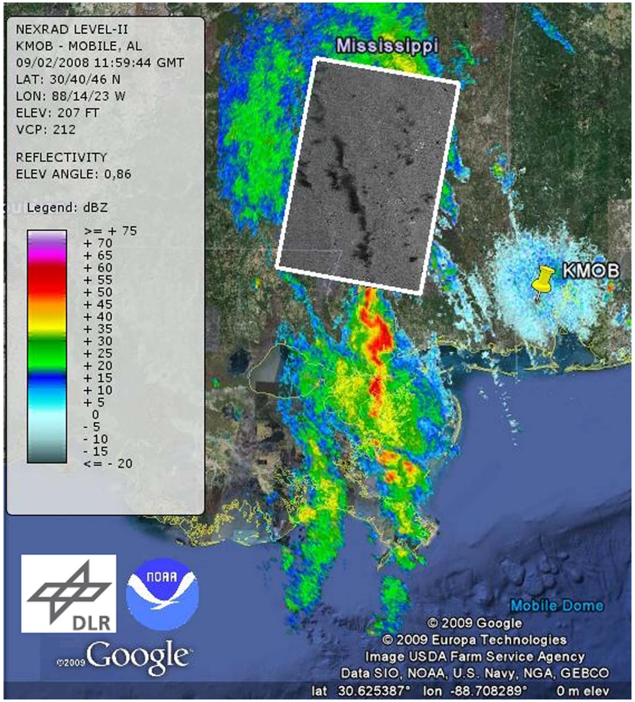

Fig. 3. Geographic representation of the NEXRAD reflectivity plan-position-indicator (PPI, in dBZ) at 0.86° elevation angle, acquired by the S-band Weather Radar (WR) near Mobile (AL, KMOB in figure) on 2 September 2008, at 12:00 UTC. The white bordered box, centered around 30.5° N × 89.5° W, represents the scene of interest acquired by TerraSAR-X (TSX) around the same time: within the box a 100 m resolution TSX quicklook is placed in arbitrary units. This image has been produced by using NOAA NCDC Weather and Climate Toolkit, TSX preview data and GoogleEarth software tools.

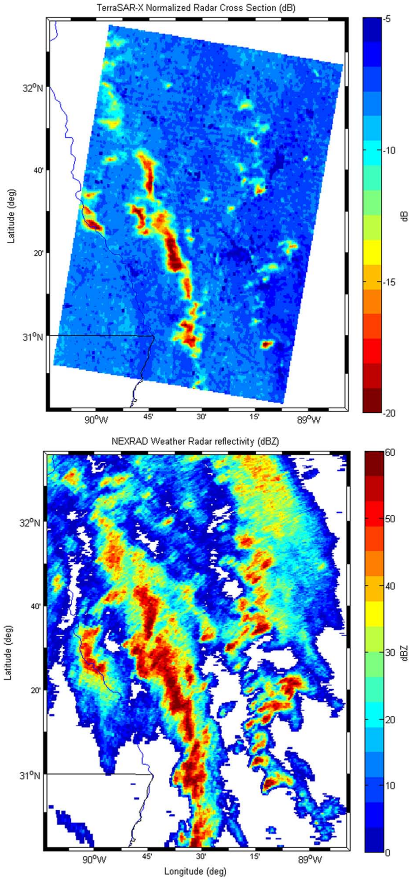

Fig. 4. (Top) TSX calibrated NRCS (dB) for the selected case study in Fig. 1. TSX data have been filtered and resampled to about 0.5 km resolution. (Bottom) Co-registered NEXRAD reflectivity factor Z PPI (dBZ) at 0.86° elevation angle at the same resolution of 0.5 km.

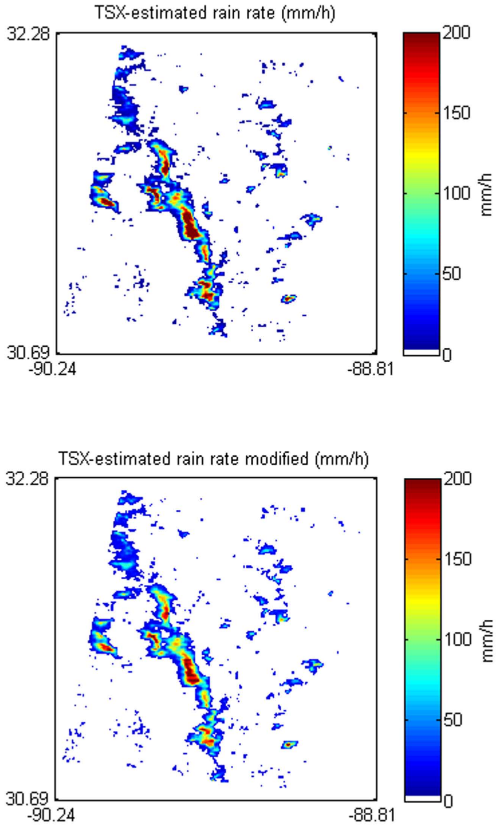

Fig. 5. (Top) TSX-estimated rain rate according to the regressive empirical algorithm (REA) approach of Eq. (3), as suggested in Marzano et al. (2010), using TSX data of Fig. 4. (Bottom) TSX-estimated rain rate according to the modified regressive empirical algorithm (MREA), given in Eq. (4). For graphical purposes scales are equally saturated at 200 mm/h, even though rain-rate values can be higher than 300 mm/h (see text).

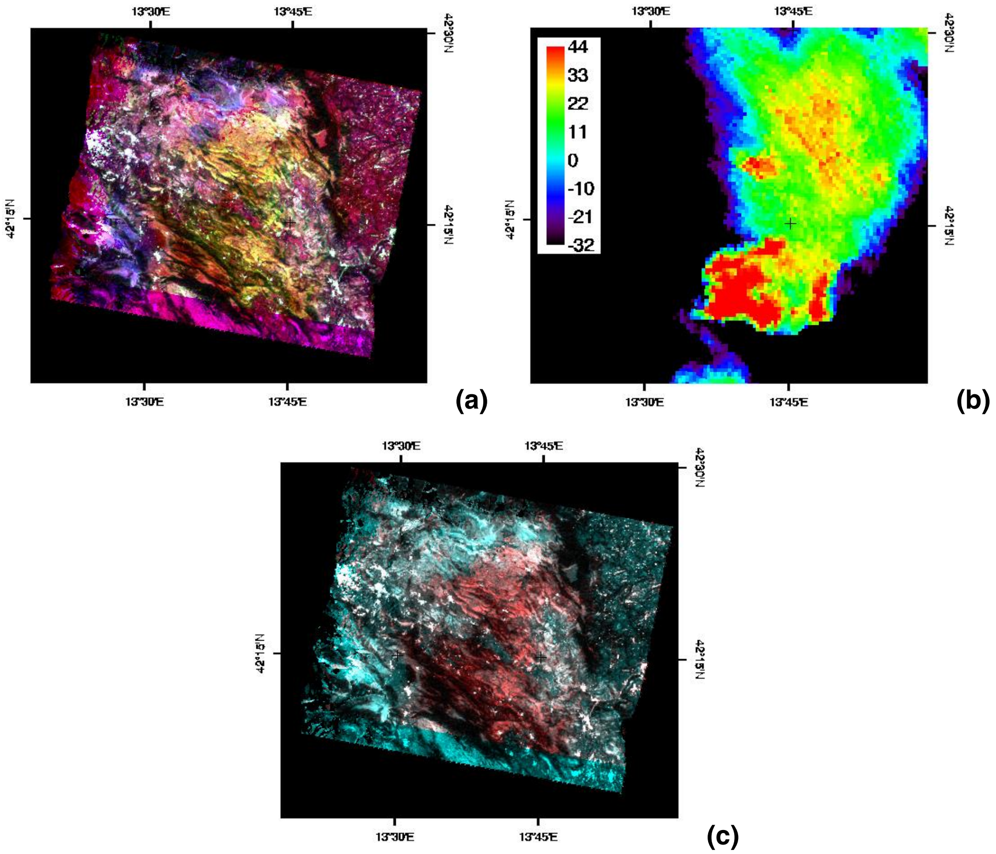

Fig. 6. Case study using CSK data over central Italy. (Left panel) Three geocoded phase coherence images are shown in an RGB color composition: Red = cc_{10-11}, Green = cc_{10-27} and Blue = cc_{11-18}. (Right panel) Precipitation map of the same area as observed by the C-band Mt. Midia weather radar in terms of reflectivity factor Z (dBZ). (Bottom panel). RGB composite of two geocoded phase coherence images (Red = cc_{10-27}, Green = Blue = cc_{11-18}).

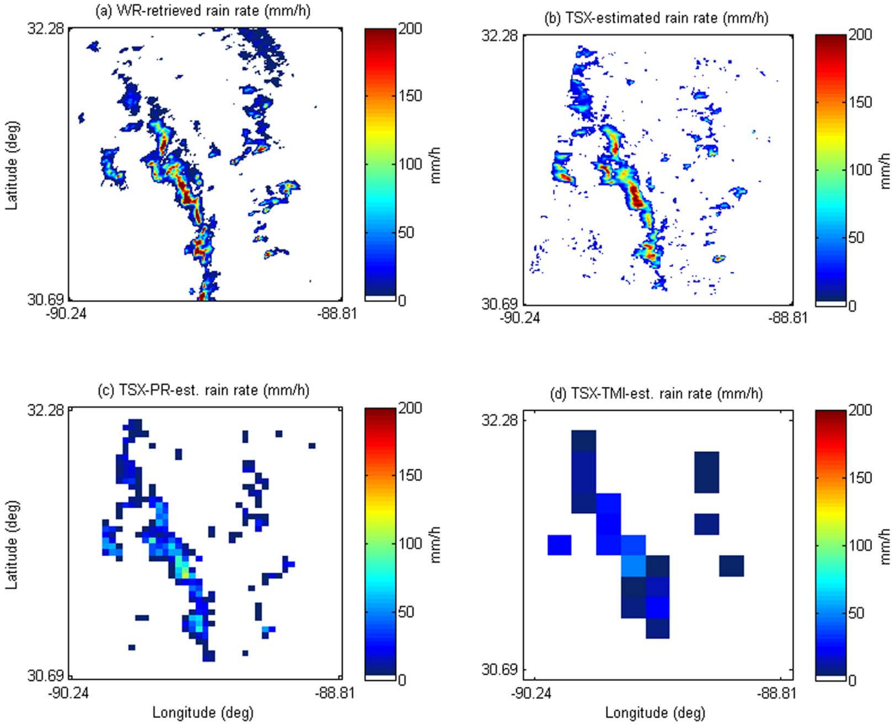

Fig. 7. (Top left) Map of measured rain rate (mm/h) obtained by standard NEXRAD Z-R relation of Eq. (5) on the WR reflectivity for the case study in Fig. 1. (Top right) Map of TSX estimated rain rate (mm/h) obtained by MREA technique in Eq. (4). (Bottom left) Map of TSX-PR estimated rain rate (mm/h) obtained by Eq. (4). (Bottom right) Map of TSX-TMI estimated rain rate (mm/h) obtained by Eq. (4). TSX-PR and TSX-TMI data are obtained by reducing resolution of the TSX data respectively at 4 km/pixel and 15 km/pixel and applying a Gaussian filter to emulate antenna pattern. TSX and WR input data are obtained from Fig. 4; note that for graphical purposes scales are equally saturated at 200 mm/h, even though WR values can be higher than 300 mm/h.

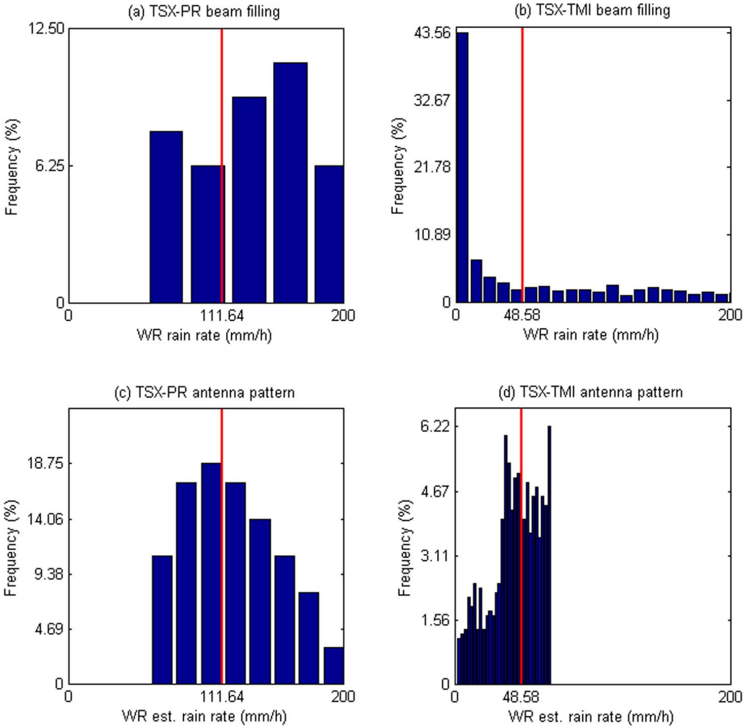

Fig. 8. Effects of the inhomogeneous beam filling and antenna pattern on TSX-PR (TSX spatial resolution reduced to that of PR) and TSX-TMI (TSX spatial resolution reduced to that of TMI) rain rate estimation within the pixel area centered at about 31.38° N × 89.33° W (high precipitation area). The plots show the histogram of WR estimated rain rate (mm/h) within the EFOV area, with (bottom) and without (top) the Gaussian filter which simulates the antenna pattern. The red bars represent the corresponding TSX-PR and TSX-TMI estimated rain rates (mm/h).

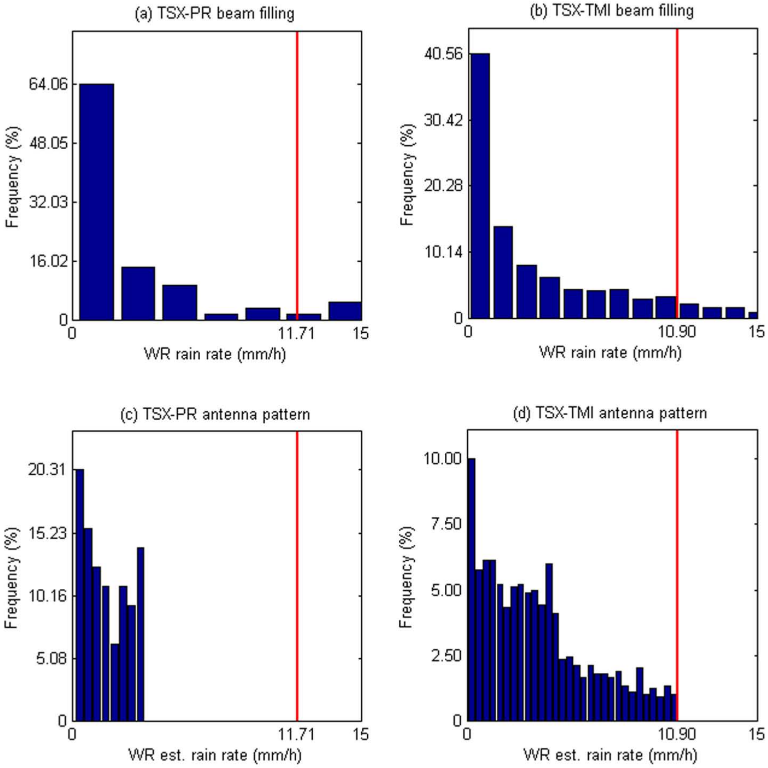

Fig. 9. Effects of the inhomogeneous beam filling and antenna pattern on TSX-PR and TSX-TMI rain rate estimation within the pixel area centered at about 31.00° N × 89.96° W (low precipitation area). The plots show the histogram of WR estimated rain rate (mm/h) within the EFOV area, with (bottom) and without (top) the Gaussian filter which simulates the antenna pattern. The red bars represent the corresponding TSX-PR and TSX-TMI estimated rain rates (mm/h).

Title Page
Abstract
Introduction
Conclusions
References
Tables
Figures
◀◀
▶▶
◀
▶
Back
Close
Full Screen / Esc
Printer-friendly Version
Interactive Discussion